Comparison of In-situ Near Infrared Melt Pool Imagery to Optical Microscopy Measurements

Joseph N. Zalameda*, Samuel J. A. Hocker, Joshua M. Fody, Wesley A. Tayon and Brodan Richter

NASA Langley Research Center Hampton, VA 23681-2199

ABSTRACT

Additive manufacturing (AM) is a rapidly growing technology. An area of major importance is the integrity and repeatability of AM parts. The goal is to reduce obstacles to certify AM built parts to allow for use in critical aerospace applications. In-situ nondestructive evaluation sensors can be used for build assessment and can potentially play a key role in certifying AM parts. For example, melt pool features are understood to have a strong correlation to microstructural defects and the use of a near infrared (NIR) camera can be used to record the melt pool, cooling areas, and temperature gradients during the build. This work explores the use of a low cost NIR camera to obtain single line track imagery of the Ti-6Al-4V melt pools for various processing parameters. The NIR camera is radiometrically calibrated and configured in-line with the laser source to obtain high resolution imagery of the melt pool shape and dynamics. The challenge to measure melt pool shapes is to identify the transition points between the metal solid to liquid phase. Factors for melt pool measurements such as thermal camera pixel resolution, surface emissivity, and blurring due to the laser beam movement are discussed. Lastly, the melt pool imagery are compared to optical microscopy measurements for validation.

Keywords: additive manufacturing, melt pool imaging, in-situ monitoring, in-line near infrared camera, optical microscopy, image deblurring

1. INTRODUCTION

Additively manufactured (AM) metal parts must be certified for broad application onto aircraft structures. One area to help certify AM parts is the use of in-situ sensors to monitor the build process. For example, an infrared camera can be used to monitor the temperature history during a laser powder bed fusion (LPBF) build. A LPBF AM process involves a laser that is scanned over a layer of metal powder. The laser is used to melt the metal powder at precise locations building a part layer by layer. From the temperature information, melt pool features can be determined and melt pool features are understood to have a strong correlation with process defects such as lack of fusion or keyhole porosity formation [1-2]. Controlling and preventing the occurrence of defects is important due to the influence they have on the part's mechanical performance [3]. The Configurable Architecture Additive Testbed (CAAT) is used to test a low cost near infrared (NIR) camera to record the thermal history.

The CAAT is used for LPBF to test various process parameters and materials. The CAAT system is a custom developed AM system that is comprised of an enclosed environmental chamber which has been modified to conduct LPBF experiments. The CAAT system allows for integration of various in-situ nondestructive evaluation (NDE) sensors as well as oxygen, humidity, and thermocouple sensors to document the build environment. The NIR camera is positioned, in-line optically with the laser, to allow for high resolution imaging of the melt pool. A calibration is performed using a blackbody radiance source. This allows conversion of the measured pixel intensity counts to radiance. If the emissivity is known, then the radiance can be converted to temperature. The melt pool boundaries can be determined from the known tempeature. Because of limited chamber space, a previous calibration involved removing some of the optical components and performing the calibration outside the CAAT chamber [4]. This was not ideal since all the optical components were not taken into consideration. In this paper we discuss a blackbody calibration where the source is placed within the chamber, and this allows for all the optical components in the optical path to be taken into account.

*joseph.n.zalameda@nasa.gov; phone 1 757-864-4793; fax 1 757-864-4914; http://nde.larc.nasa.gov

In addition to the radiance calibration, other factors are required to measure melt pool width. These include the thermal camera pixel resolution, selection of the solidus temperature, and appropriate emissivity value. In addition, any blurring due to movement of the laser in relation to the camera's integration time will need to be taken into account. The measured melt pool width from the radiance images are compared to optical microscopy results. Ex-situ optical microscopy is obtained by serial sectioning at different locations along the melt line. The cross section is mechanically polished and etched to visually reveal the melt areas.

2. ADDITIVE MANUFACTURING AND MEASUREMENT SYSTEM DESCRIPTION

2.1 Configurable Architecture Additive Testbed (CAAT)

The CAAT system is comprised of an enclosed environmental chamber that has been modified to conduct LPBF experiments with a variety of sensors and multiple view port windows for various camera configurations. Shown in Figures 1(a) and 1(b) are a picture of the CAAT system and drawing respectively. The environmental chamber is fitted with sensors such as oxygen sensors (< 10 ppm operation), a humidity sensor, and thermocouples. The laser source was an IPG Model YLR-1000-WC-Y14, with a modulated continuous emission wavelength of 1070 nm and a maximum power of 1 kW. The scan system was a SCANLAB GmbH IntelliSCAN III 20 with a LINOS F-Theta-Ronar lens with a 255 mm focal length. The in-line (coaxial to the laser heat source) camera sensor setup is shown in Figure 2. The setup shows beam splitter #2 which splits the light for the two infrared cameras; however, for this study only one NIR camera (camera #2) was used. The camera field of view follows the laser path using the SCANLAB GmbH camera adapter that consists of a focusing objective and a beam splitter #1. This coaxial method is used to obtain the highest resolution imagery of the melt process. The beam splitter #1 separates the 1070 nm laser beam from NIR wavelengths that are measured by the camera.

The in-line camera used is a low-cost Basler acA640-750um camera. This camera has an ON-Semiconductor CMOS sensor, a 4.8 x 4.8 um pixel pitch, a 640 x 480 pixel array, a dynamic range of 10 bits, and a maximum frame rate of 751 Hz at full pixel resolution. The spectral sensitivity of the sensor is shown in Figure 3, which shows the sensor's relative response at 900 nm is approximately 30 percent and at 1000 nm is approximately 10 percent. Thus, the sensor is adequate for NIR measurements. The camera's optical path was configured with an 880 nm narrow band filter with a bandwidth of 875 to 884 nm. This narrow band was selected to reduce signal saturation due to the camera's limited dynamic range and to further reduce the potential of laser reflections damaging the detector. A drawback however is the reduced sensitivity to lower temperatures.

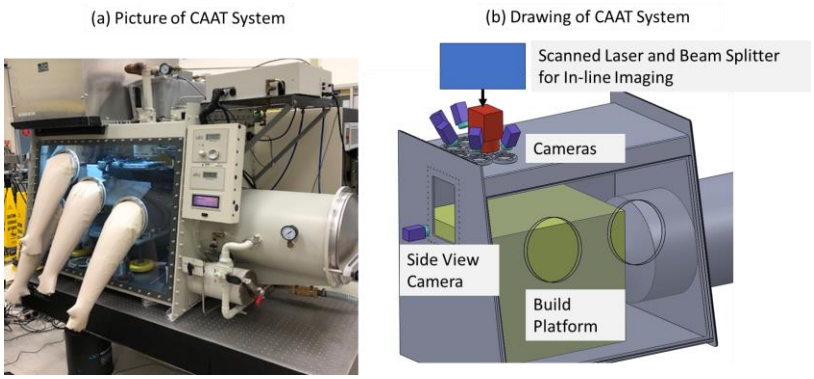

Figure 1: CAAT system setup (a) picture of system and (b) drawing of test setup.

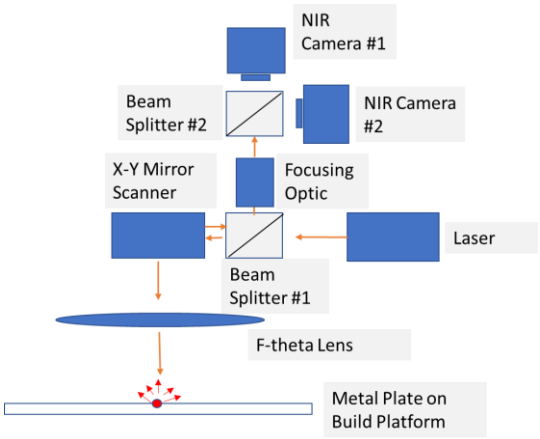

Figure 2: In-line NIR camera setup.

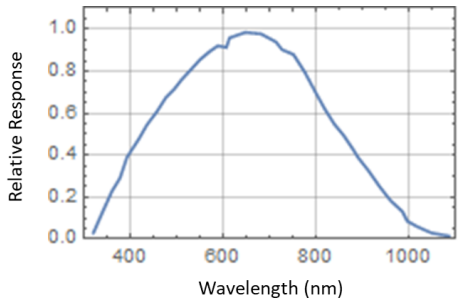

Figure 3: In-line camera sensor relative response.

2.2 Calibration of NIR Camera Sensor

The coaxial NIR camera was calibrated to obtain radiometric imagery of the metal melt pool. A blackbody calibration technique was necessary to calibrate the pixel intensity counts to radiance. The calibration setup shows the blackbody within the build chamber in Figure 4. The blackbody radiation source (Mikron M335) was varied in temperature: 900, 1000, 1100, 1200, 1300, 1400, and 1500 degrees Celsius. For each temperature, the integration time was varied at the following values: 59, 75, 100, 150, 300, 500, 700, 900, 1200, and 1,500 microseconds and an averaged pixel intensity counts was obtained from the image center.

The effective radiance measured from the blackbody source to the camera's sensor is determined using equation (1) which is Planck's blackbody radiation equation. The in-band radiance is defined by the filter used and is 875 to 884 nanometers. The filter response is estimated to be a top hat function with 95 percent transmission over the bandpass. The response is taken into account in equation (1) by linear interpolation of the sensor's relative response (Figure 3) over the wavelength band.

$$Effective\ Radiance = \frac{1}{2}\int_{\lambda_1}^{\lambda_2} \frac{c_1}{\lambda^5\left(e^{\frac{c_2}{\lambda\,(T+273.15)}}-1\right)} * sensor(\lambda) * filter(\lambda) * d\lambda \quad \text{where } c_1 = 2 * h * c^2 \quad \text{and} \quad c_2 = \frac{h * c}{k} \qquad (1)$$

For equation (1), λ is the wavelength variable, λ_1 and λ_2 are the wavelength bounds of 875 to 884 nanometers respectively, and T is temperature in degrees Celsius. The effective radiance is divided by 2 to account for the light split at beam splitter #2. The constants c_1 and c_2 are a function of the speed of light (c = 2.99792 x 10^{17} nanometers/second), Plank's constant (h = 6.26 x 10^{-16} nanometers^2 kilogram/second), and Boltzmann's constant (k = 1.3806 x 10^{-5} nanometers^2 kilogram/second^2//Kelvin). From equation (1) the blackbody temperature versus the effective radiance is calculated over a range of 900 to 1900 degrees Celsius as shown in Figure 5, and therefore for each intensity versus integration time curve

in Figure 6(a), the radiance is known. Shown in Figure 6(b) is the count rate (pixel intensity over integration time obtained from Figure 6(a)) versus the effective radiance.

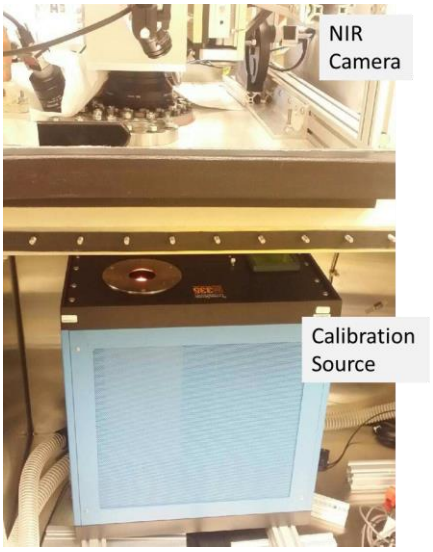

Figure 4: In-line camera sensor calibration setup with blackbody source within the build chamber.

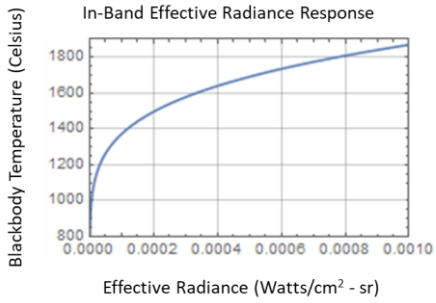

Figure 5: The blackbody temperature vs. in-band effective radiance response of the CAAT optical path and sensor.

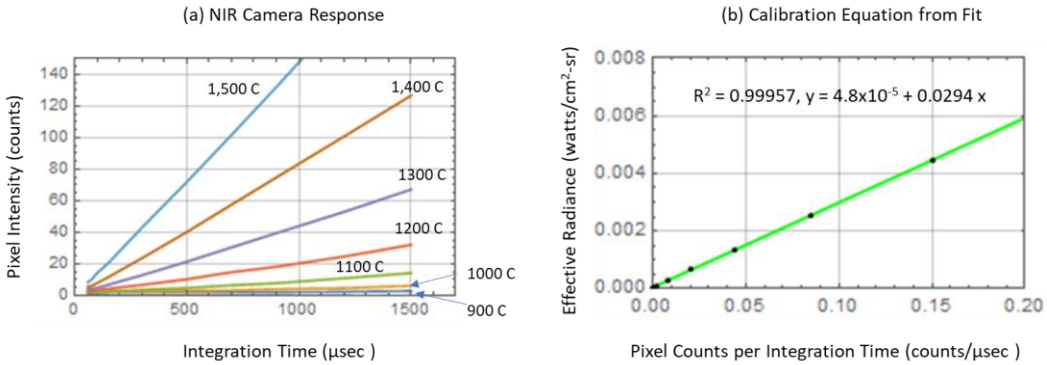

Figure 6: In-line camera sensor blackbody calibration results with conversion to effective radiance.

As expected, the response is highly linear with an R squared value of 0.99957. The calibration equation is given as: Effective Radiance = 4.8 x10^{-5} + 0.0294* ((counts – dark value)/integration time). The dark value, measured with the lens covered, was on average around 3 counts. For a given integration time and camera pixel counts (dark offset counts subtracted), the camera's pixel intensity counts can then be converted to effective radiance imagery.

3. MEASUREMENT RESULTS

3.1 Melt Pool Imaging of Ti-6Al-4V Plate

The in-line NIR camera was used to obtain imagery of the metal melt pool on a Ti-6Al-4V plate. The top-down microscope image of a single line track is shown in Figure 7 for laser power of 280 Watts and scanning speed of 500 mm/sec. The solid plate thickness is approximately 2.5 mm. Various laser scan tracks of power and scanning velocities were used to generate melting at the surface.

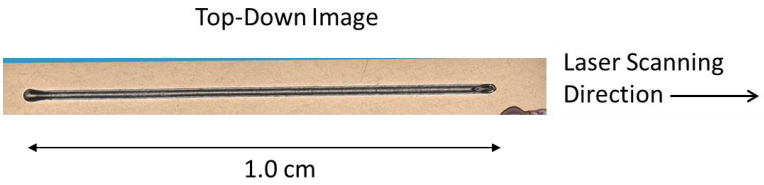

Figure 7: Top-down photograph of Ti-6Al-4V test plate used for CAAT testing.

Shown in Figure 8 are example laser generated melt pool images of the Ti-6Al-4V metal plate. The laser heating power of 280 Watts and laser scanning speeds of 500, 850, and 1200 mm/second were used. The images were selected in the middle of the laser scan path to ensure the laser scanning speed is constant and that the thermal profiles have reached steady state. The images were obtained at a frame rate of approximately 2,000 Hz with pixel array dimensions of 144 x 144, a 10 bit dynamic range, and with a camera integration time of 200 µs. The pixel resolution using a calibrated target was determined to be approximately 8.55 µm/pixel and therefore the image field of view is approximately 1.2 x 1.2 mm^2. Also shown in Figure 8 are a comparison of the vertical line plots over the center of the melt pools for the various laser scanning velocities. As expected, the faster the laser scanning speed, the lower the energy delivered per mm resulting in a smaller melt pool width. The laser power was constant at 280 Watts and the energies delivered for velocities of 500, 750, and 1200 mm/second were 0.56, 0.37 and 0.23 Joules/mm respectively.

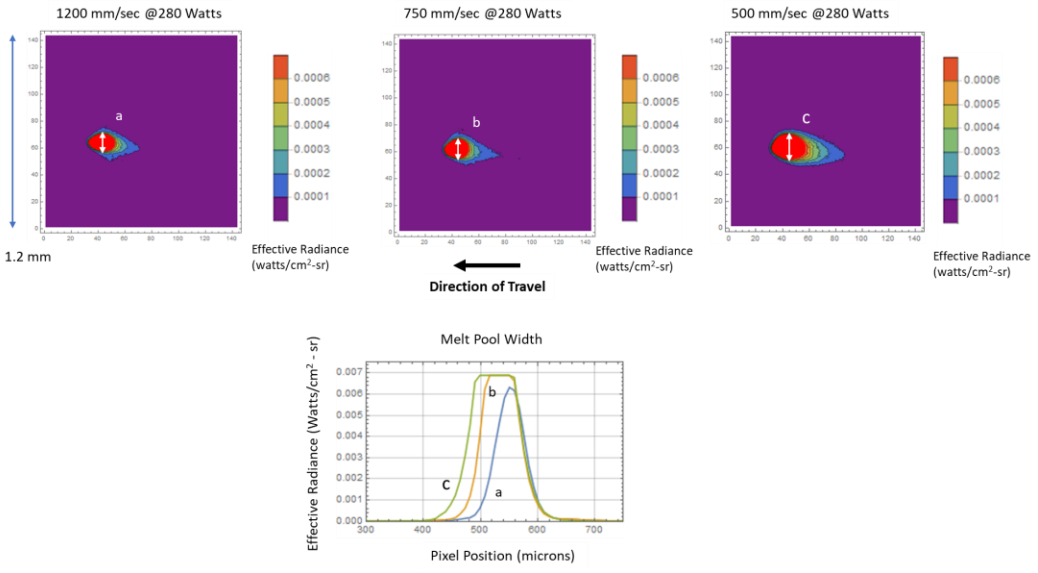

Figure 8: Camera melt pool imaging for various laser scan velocities with corresponding line plots over the melt pool center.

3.2 Melt Pool Imaging Comparison to Optical Microscopy

The calibration was used to obtain radiometric imagery of the metal melt pool along the scan track. The pixel intensity counts are converted to effective radiance and dividing by the known emissivity allows conversion to estimated temperature. The estimated solidus temperature boundary of 1605 degrees Celsius [5] can then be located. The emissivity of Ti-6Al-4V can vary with values of 0.40, 0.48, and 0.58 [6-9]. An emissivity of 1.0 is a perfect emitter and is used for a comparison. From the calibration, the corresponding pixel intensity counts thresholds were determined and are given as follows: emissivity = 0.40 threshold pixel intensity counts = 24 (radiance = 0.00299 Watt/cm^2 sec), emissivity = 0.48 threshold pixel intensity counts = 27 (radiance = 0.00358 Watt/cm^2 sec), emissivity = 0.58 threshold pixel intensity counts = 32 (radiance = 0.004339 Watt/cm^2 sec) and emissivity = 1.0 threshold pixel intensity counts = 53 (radiance = 0.00741 Watt/cm^2 sec). Shown in Figures 9 and 10 are the melt pool widths determined from the NIR camera imagery for laser scanning velocities of 500 mm/sec and 750 mm/sec respectively for various emissivity values of 0.40, 0.47, 0.58, and 1.0. The melt pool widths, determined from the NIR camera imagery, are larger at the start of the scan and reaches a relatively steady value along the track to the end. This is due to the startup velocity of the laser. Also shown in Figures 9 and 10, are the cross-sectional optical microscopy measurements. Ex-situ optical microscopy is used to visually measure the width of the melted zone at various locations along the center of the scan track. The optical microscopy measurements were obtained on an inverted optical microscope at a magnification of 500x. Each track was sectioned along the scan track. Prior to imaging, samples were mechanically polished and etched with Kroll's reagent (93 mL distilled water, 6 mL HNO3, 1 mL HF) to reveal the underlying microstructure for melt pool width measurement. The optical microscopy results are in poor agreement for the emissivity curves as shown in Figures 9 and 10. It was expected that the optical microscopy measurements would be between the acceptable range of emissivity from 0.40 to 0.58. To improve the agreement the image blur must be taken into account, and this is discussed in the next section.

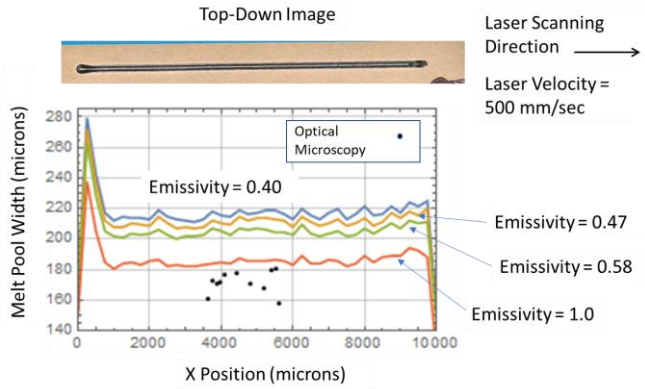

Figure 9: Laser scanning speed of 500 mm/sec comparison of cross-sectional optical microscopy melt pool width measurements with thermal imaging melt pool width for various values of emissivity.

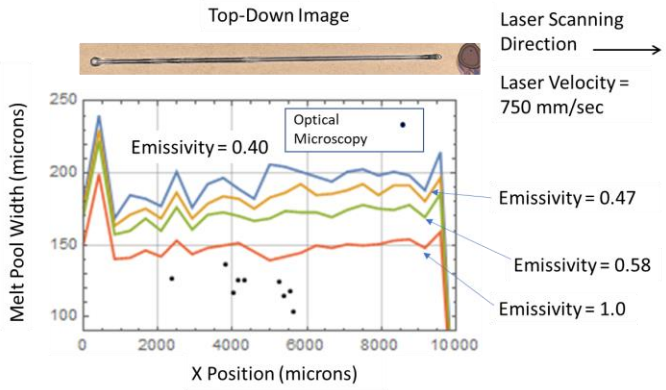

Figure 10: Laser scanning speed of 750 mm/sec comparison of cross-sectional optical microscopy melt pool width measurements with thermal imaging melt pool width for various values of emissivity.

3.3 Image Blur Removal for Melt Pool Imaging

The camera integration time was set to 200 µs and given the laser scanning velocity, significant blurring can occur. For example, for a laser scanning velocity of 500 mm/sec and with pixel resolution of 8.55 µm the pixel blur can be approximately 12 pixels and for a laser scanning velocity of 750 mm/sec the pixel blur can be approximately 18 pixels. A Weiner inverse filtering technique is commonly used to remove image motion blur [10]. The inverse filter is based on the direction of scanning in addition to the blur length. This computation can easily be done in the Fourier transform frequency domain and the equation used is given in (2).

$$Deblurred\ Image(u,v) = W(u,v)Blurred\ Image(u,v) \quad \text{where} \quad W(u,v) = \frac{H^*(u,v)}{|H(u,v)|^2 + K(u,v)} \qquad (2)$$

The Fourier transform of the blurred image is multiplied by the Weiner filter $W(u,v)$. The Weiner filter, $W(u,v)$, is equal to the complex conjugate, $H^*(u,v)$, of the blurring function image representing a horizontal bar of 12 pixels (500 mm/sec scanning speed) or 18 pixels (750 mm/sec scanning speed) in the image center, $|H(u,v)|^2$ is the magnitude of the blur function image, and $K(u,v)$ is a parameterized factor proportional to the inverse of the blurred image signal to noise. Typically, $K(u,v)$ is set to a scalar factor and is determined empirically. The values of K = 0.12 and K = 0.27 for the 500 mm/sec and 750 mm/sec laser scanning velocities were used. The values of K were determined iteratively by visually minimizing the lower temperatures difference and image distortions. If the value of K is too low the filter produces image distortions and if the value K is too high the lower temperatures will not agree. The inverse Fourier transform of the filtered image produces the final filtered or deblurred image in the spatial domain. Shown in Figure 11 is a blurred and deblurred image for laser scanning speed of 500 mm/sec and camera integration time of 200 µs. The right plot shows the width is smaller for the deblurred image. It is noted that even though the direction of laser travel is perpendicular to the melt pool width, there still is an influence of blurring. The importance of deblurring would be more emphasized for melt pool area measurements.

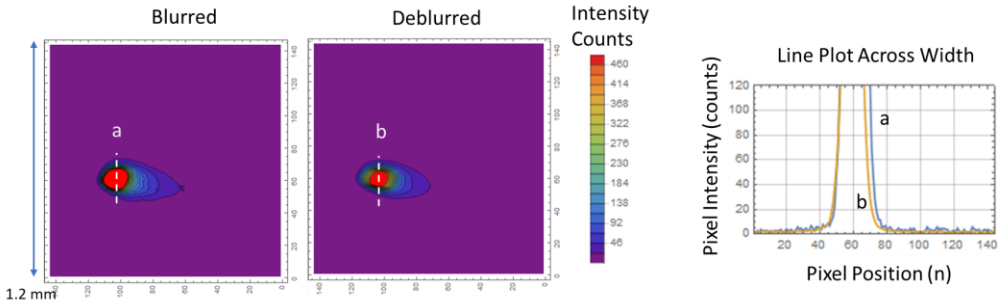

Figure 11: Comparison of blurred and deblurred image with line plot across width.

3.4 Deblurred Melt Pool Imaging Comparison to Optical Microscopy

Shown in Figures 12 and 13 are the deblurred melt pool widths for laser scan velocities of 500 mm/sec and 750 mm/sec respectively. The NIR camera measurement of melt pool widths for various emissivity values of 0.40, 0.47, 0.58, and 1.0 are also shown in Figures 12 and 13 along with the cross-sectional optical microscopy measurements for a comparison. The agreement is improved with some of the optical microscopy measurements approaching the 0.58 emissivity curve for the 500 mm/sec measurements. The NIR data appears to be overpredicting the width for the 500 mm/sec laser scan velocity. The optical microscopy measurements are spread between the 0.40 and 0.58 emissivity curves for the 750 mm/sec laser scanning speed. One possible source of errors, for the NIR measurements, is that the calibration would need to be performed for higher temperatures. Also it is expected that optical microscopy measurements would be less scattered and more aligned with a single emissivity curve for both velocities. The optical microscopy measurement errors are discussed in the next section.

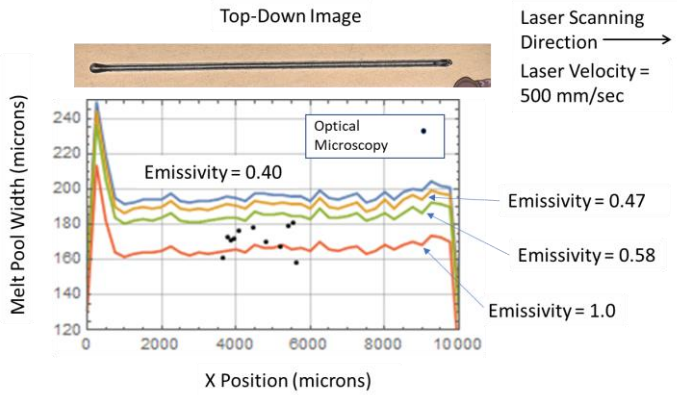

Figure 12: Laser scanning speed of 500 mm/sec comparison of cross-sectional optical microscopy melt pool width measurements with deblurred thermal melt pool width for various values of emissivity.

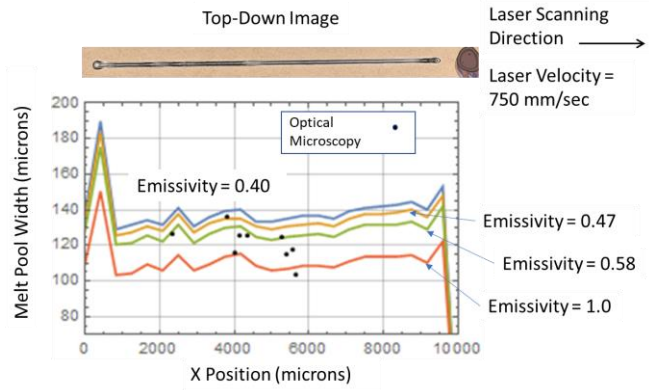

Figure 13: Laser scanning speed of 750 mm/sec comparison of cross-sectional optical microscopy melt pool width measurements with deblurred thermal melt pool width for various values of emissivity.

3.5 Optical Microscopy Errors

The scatter of the optical microscopy melt pool width results appears to be quite significant. This could be attributed to the difficulty in visually measuring the melt pool width. This is shown in Figure 14 where the boundaries of the melted and non-melted areas are not clearly defined. This is illustrated in the yellow markers showing the melt pool width determined by looking at the top-down image instead of the cross sectioned image. The potential errors in the melt pool widths determined from the cross-sectional imaging appears to be significant and perhaps this explains the significant scatter in the optical microscopy measurements. This area will need to be investigated further to determine the effectiveness of using the NIR imagery to determine melt pool width. It appears in Figure 14, however, that the melt pool depth is clearly defined.

4. CONCLUSIONS

A low cost NIR camera was used to obtain single line track imagery of Ti-6Al-4V melt pools for various processing parameters. The NIR camera was configured in-line with the laser source to obtain high resolution imagery of the melt pool shape. The challenge, using a single NIR camera to measure the melt pool width, is to identify the transition points between the metal solid-to-liquid phase. This involves selection of the proper emissivity value. In addition, as demonstrated in this work, blurring must be taken into account if the camera's integration time is slow relative to the laser scanning speed. It seems that further investigation of optical microscopy errors will need to be addressed to allow for a more accurate comparison to the NIR melt pool imaging results.

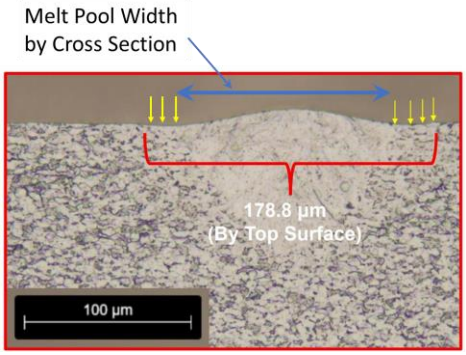

Figure 14: Measurement of melt pool width using optical microscopy.

ACKNOWLEDGEMENTS

This work was done under the NASA Aeronautics Research and Mission Directorate's Transformational Tools and Technologies (TTT) additive manufacturing project.

REFERENCES

[1] Yap, C.Y., Chua, C.K., Dong, Z.L., Liu, Z.H., Zhang, D.Q., Loh, L.E., and Sing, S.L., Review of Selective laser melting: Materials and applications, Applied Physics Reviews 2, 041101 (2015); doi:10.1063/1.4935926.

[2] Everton, S., Hirsch, M., Stravroulakis, P., Leach, R., and Clare, A., "A Review of in-situ process monitoring and in-situ metrology for metal additive manufacturing", AI, Materials & Design, vol. 95, April 2016.

[3] Soltani-Tehrani, A., Shrestha, R., Phan, N., Seifi, M., & Shamsaei, N. (2021). Establishing specimen property to part performance relationships for laser beam powder bed fusion additive manufacturing. International Journal of Fatigue, 151, 106384.

[4] Zalameda, J. N., Hocker, S. J., Fody J. M., Tayon, W. A., "Melt pool imaging using a configurable architecture additive testbed system", Proc. SPIE 11743, Thermosense: Thermal Infrared Applications XLIII, 117430E (12 April 2021); doi: 10.1117/12.2585791.

[5] Solidus Temperature of Ti-6Al-4V,Titanium alpha-beta alloy, Grade 5 (Ti-6Al-4V) [SubsTech], accessed March 2022.

[6] Emissivity of Ti-6Al-4V as a Function of Temperature, TIMETAL 6-4 (spacematdb.com), accessed March 2022.

[7] Touloukian, Y. and DeWitt, D., "Thermophysical Properties of Matter, Volume 7, Thermal Radiative Properties," Met. Elem. Alloy. York IF Plenum), 1970.

[8] Khairallah, S. A., Anderson, A. T., Rubenchik, A. and King, W. E., "Acta Materialia Laser powder-bed fusion additive manufacturing: Physics of complex melt flow and formation mechanisms of pores, spatter, and denudation zones," Acta Mater., vol. 108, pp. 36–45, 2016, doi: 10.1016/j.actamat.2016.02.014.

[9] Boivineau, M., et al., "Thermophysical properties of solid and liquid Ti-6Al-4V (TA6V) alloy," Int. J. Thermophys., vol. 27, no. 2, pp. 507–529, 2006, doi: 10.1007/PL00021868.

[10] Gonzalez, R. C. and Woods, R. E., Digital Image Processing (3rd Edition). Prentice Hall, August 2007.